Asian Journal of Chemistry; Vol. 34, No. 9 (2022), 2288-2296

ASIAN JOURNAL OF CHEMISTRY

https://doi.org/10.14233/ajchem.2022.23840

Influence of Ce^{3+} Substitution on Magnetic Properties and Antibacterial Activity of Manganese Ferrite Nanoparticles Synthesized by Coprecipitation Method

A. PRAKASH[1], R. SAGAYARAJ[2,*], D. JAYARAJAN[3], S. ARAVAZHI[1,*], G. CHANDRASEKARAN[4] and R. NITHYA[5]

[1]Department of Physics, Arignar Anna Government Arts College (Affiliated to Thiruvalluvar University), Villupuram-605602, India
[2]PG & Research Department of Physics, St. Joseph's College of Arts and Science (Autonomous) (Affiliated to Annamalai University), Cuddalore-607001, India
[3]Department of Microbiology, Divine Mother College, Korkadu, Pondicherry-605110, India
[4]Department of Physics, Pondicherry University, Pondicherry-605014, India
[5]Department of Physics, Immaculate College for Women (Affiliated to Annamalai University), Cuddalore-607007, India

*Corresponding authors: E-mail: ara_vazhi@yahoo.co.in; sagayarajnancy@gmail.com

Received: 19 March 2022; *Accepted*: 1 June 2022; *Published online*: 19 August 2022; AJC-20924

Rare earth element cerium incorporated $MnFe_2O_4$ nanoparticles were synthesized by using a co-precipitation method. Phase signature, vibrational analysis, morphology, element composition, magnetometry, surface analysis, medicated analysis were studied by XRD, FTIR, FE-SEM, EDAX, VSM, XPS and antibacterial activity. X-ray diffraction (XRD) reveals a cubic structure and obtained crystallite size and lattice constant. Fourier transform infrared spectroscopy (FTIR) studies were confirmed spinel structure ferrite. Vibrating sample magnetometer (VSM) revealed that the magnetic interaction of materials and obtained saturation magnetization, remnant magnetization and coercivity, which were impressed by their magnetic properties by Ce^{3+} incorporated $MnFe_2O_4$. Field emission scanning electron microscope (FE-SEM) observed clear lattice size and magnetic domain nature. X-ray photoelectron spectroscopy (XPS) confirmed cerium (Ce^{3+}) ions in the all doped materials and identified the chemical state of ions in the ferrite composite. Antioxidant effects were observed against Gram-positive and Gram-negative bacteria ferrite nanoparticles.

Keywords: Cerium, Ferrite nanoparticles, Antibacterial activity, Magnetization, Co-precipitation method, Nanoparticles.

INTRODUCTION

In literature, a strong antibacterial activity of CeO_2 and its doped ferrite nanoparticles is observed, which lead novel approaches in the production of biomedical, food applications and antimicrobial control systems. Cerium oxide nanoparticles with cubic fluorite phase/structure have improved antibacterial activity and band gap is 2.61 eV [1]. CeO_2 nanoparticles have a unique antibacterial activity because of their reversible conversion between (pro-oxidant & antioxidant) Ce^{3+} and Ce^{4+} valence states. For the reactive oxygen species (ROS) involved in the antibacterial activity mechanism, where Ce^{3+} occupy octahedral voids and O^{2-} occupy tetrahedral voids. The CeO_2 nanoparticles can destroy cancer cells by causing them to produce free radicals because of reactive oxygen species (ROS) [2]. It is hypothesized that CeO_2 nanoparticles' antibacterial activity is effective since the cellular proteins being inactive after successfully incorporating pathogens, causing their enzymes to become deactivated and the pathogens to die [3]. The Ce^{3+}/Ce^{4+} ratio is used to assess the concentration of oxygen vacancies. As a result, nanoparticles as a functionalized percentages of cerium particles increase as particle sizes decrease and *vice-versa*. Because of the oxygen vacancy, a quantified region known as oxygen storage capacity arose. An improvement in this ratio favours ROS, but a decrease favours catalytic activity.

CeO_2 is also a natural insulator and it exists as Ce^{4+} ions. As a result, it exhibits diamagnetic behaviour. However, CeO_2 nanoparticles have a ferromagnetic character and magnetic analysis suggests that Ce^{3+} ions have their own magnetic moment unlike Ce^{4+} ions [4].

$$3Ce^{4+} + 3O^{2-} \longrightarrow 3Ce^{3+} + 3O_2 \text{ (reduction)}$$

$$Ce^{3+} + O^{2-} + 2H^{+} \longrightarrow Ce^{4+} + H_2O_2 \text{ (oxidation)}$$

Positively charged nano-cerium particles (Ce^{3+} or Ce^{4+}) are well absorbed on bacterial cells because of electrostatic interaction. Cellular proteins become inactive because of this interaction and nano-cerium particles penetrate the bacterial cell wall, deactivating bacterial enzymes and causing hydrogen peroxide formation. After absorption, bacterial wall membrane oxidation will reduce nano-cerium particles from Ce^{4+} to Ce^{3+} on the cell surface, causing oxidative stress [5]. When cells are treated as nanoparticles, ROS is a potential oxidative stress within the cells and it is a major cause of cell death. For Gram-positive and Gram-negative bacteria strains, pH > 9 resulted in the development of reactive oxygen species (ROS) and a higher pH was the most effective treatment in inhibiting bacteria growth. Under these circumstances, ROS production was detected [6].

The magnetic characters of the synthesized materials were altered when manganese was doped on $CeFeO_3$. Consequently, all electrons are paired and Ce^{4+} is non-magnetic, which characterizes diamagnetic nature. However, the antiferromagnetic order of Fe^{3+} ions is largely occupied by octahedral sites, resulting in weaker ferromagnetism. Hence spin canted iron ions (Fe^{3+}/Fe^{2+}) and disordered surface spins, which exhibit poor ferromagnetic properties. The presence of oxygen vacancies disrupts anti-parallel spin ordering in Fe^{3+}–O^{2-}–Fe^{3+} by super-exchange interactions [7]. Generally, cerium ions (Ce^{3+}) are resting on the octahedral site, while it has enough space for Ce^{3+} ions and its large ionic radius (1.14 Å). The effect of Ce^{3+} non-magnetic ions doped in ferrites, which rearrangement ions were formed between the two crystallographic sites. Since materials have different structural parameters [8]. For magnetic properties, synthesized ferrites are strongly dependent on temperature and crystallite size. Cerium incorporated ferrite materials have large applications. Since, it has redox couple ($Ce^{4+} \rightarrow Ce^{3+}$) behaviour. These redox characters can be used in fuel cells, hybrid solar cells and humidity sensing and oxygen storage devices as reported by many researchers [9]. Ce^{3+} ions substituted in the magnesium ferrite, which creates oxygen vacancies causes decreases the intensity of peaks and also shift to peaks towards lower diffraction angles. The large Ce^{3+} ions tend to occupy octahedral sites, which lead to the migration of Fe^{3+} ions from octahedral site to tetrahedral sites [9]. The lattice strain defects due to loss of oxygen with imbalance cations of spinel matrix. These defects may arise in doping ions, temperature, surface stress and oxygen fractional pressure [10]. When Ce^{3+} ions occupy octahedral sites, then the net magnetization decreases according to the ions distribution model. There are three interactions functionalized in the materials, such as A–A, B–B and A–B interactions. In which A–A and B–B interactions are weaker, then A–B interactions [11].

The microbial colonies are mostly influenced by particle size and surface area. Cerium mixed magnetic oxide nanoparticles exhibit better antibacterial microbial colonies [12,13]. The cell wall of Gram-negative bacteria is substantially thinner (2 to 8 nm) than that of Gram-positive bacteria (20 to 80 nm). Negatively charged ions can penetrate cell membranes more effectively. The Gram-positive bacteria's surface has less negatively charged ions (electrostatic force). The outer membrane permeability barrier of Gram-positive bacteria is more complicated than that of Gram-positive. As a result, Gram-negative bacteria are more drug resistant than Gram-positive bacteria. Nanoparticles infiltrate the membrane's surface (DNA, RNA, protein, lipids and enzymes), forming microbial colonies and killing microorganisms [14-16]. The surface nature of Gram-positive bacteria is negatively charged. Electrostatic attraction allows positively charged cerium (Ce^{3+}) nanoparticles to quickly absorb bacterial membranes. The most important aspect in its antibacterial action is this force. These show excellent antibacterial activity due to the production of reactive oxygen species against Gram-positive and Gram-negative bacteria [17,18]. Over all this work reflects controlled crystallite size, morphological characteristics, magnetic properties and antibacterial effect.

EXPERIMENTAL

Anhydrous ceric sulfate [$Ce(SO_4)_2$], manganese(II) sulfate heptahydrate ($MnSO_4 \cdot 7H_2O$), ferric sulfate monohydrate ($Fe_2(SO_4)_3 \cdot H_2O$, 99%), polyvinyl pyrrolidone (PVP), 98%) ethanol and ammonia were procured from Sigma-Aldrich, USA.

Synthesis of $Mn_{1-x}Ce_xFe_2O_4$: $Mn_{1-x}Ce_xFe_2O_4$ mixed ferrites were employed by low-cost co-precipitation method. Fig. 1 simply explains the preparation of cerium doped manganese ferrite. Annealing temperature, concentration, potential hydrogen (pH) and stirring time are significant to make spinel ferrite while MCF powders desired shapes and size of particles. The precursors were mixed of stoichiometric ratio as 1:2. For pH level, maintained at 11 when NH_3 was added to the mixer. Now, ferrite solution is observed black colour [19]. Ferrite solution well stirred for 4 h at 70 ºC by magnetic stirrer. Finally, ethanol and pure water were used to remove the unwanted materials and washing purposes by centrifuge. The precipitate was washed thoroughly and dried in oven at 100 ºC for 4 h. and then annealed at 600 ºC for 4 h using muffle furnace. The co-precipitation reaction and ferrite formation are furnished as follows:

Co-precipitation:

$$(1)\ Mn^{2+} + (x)Ce^{4+} + (2\text{-}x)Fe^{3+} + OH^- \rightarrow$$
$$(1)\ Mn(OH)_2 \cdot (x)Ce(OH)_2 \cdot (2\text{-}x)Fe\ (OH)_3$$

Ferrite step:

$$(1)\ Mn(OH)_2 \cdot (x)\ Ce(OH)_2 \cdot (2\text{-}x)Fe(OH)_3 \rightarrow$$
$$(1)\ Mn_{1-x}Ce_xFe_2O_4 + 5H_2O$$

Antibacterial activity: Cerium doped manganese ferrite nanoparticles were evaluated against Gram-positive bacteria and Gram-negative bacteria. *Enterobacter cloacae*, *Escheichia coli*, *Staphylococcus haemolyticus* were grouped as Gram-positive bacteria while *Staphylococcus petrasii subs. pragensis*, *Bacillus subtilis* and *Bacillus cereus* were grouped as Gram-negative bacteria . These cultures were grown on an effective platform at 37 ºC for overnight incubation and then refrigerated at 4 ºC. Well diffusion method (5 Mm) was used at various concentrations (100, 75, 50, 25 and 12.5 µg/mL). Pure cultures of bacterial pathogens were subcultured in an appropriate medium. Ciprofloxacin as standard (10 g) was used a control. The zones of inhibition were measured after 24 h at 37 ºC.

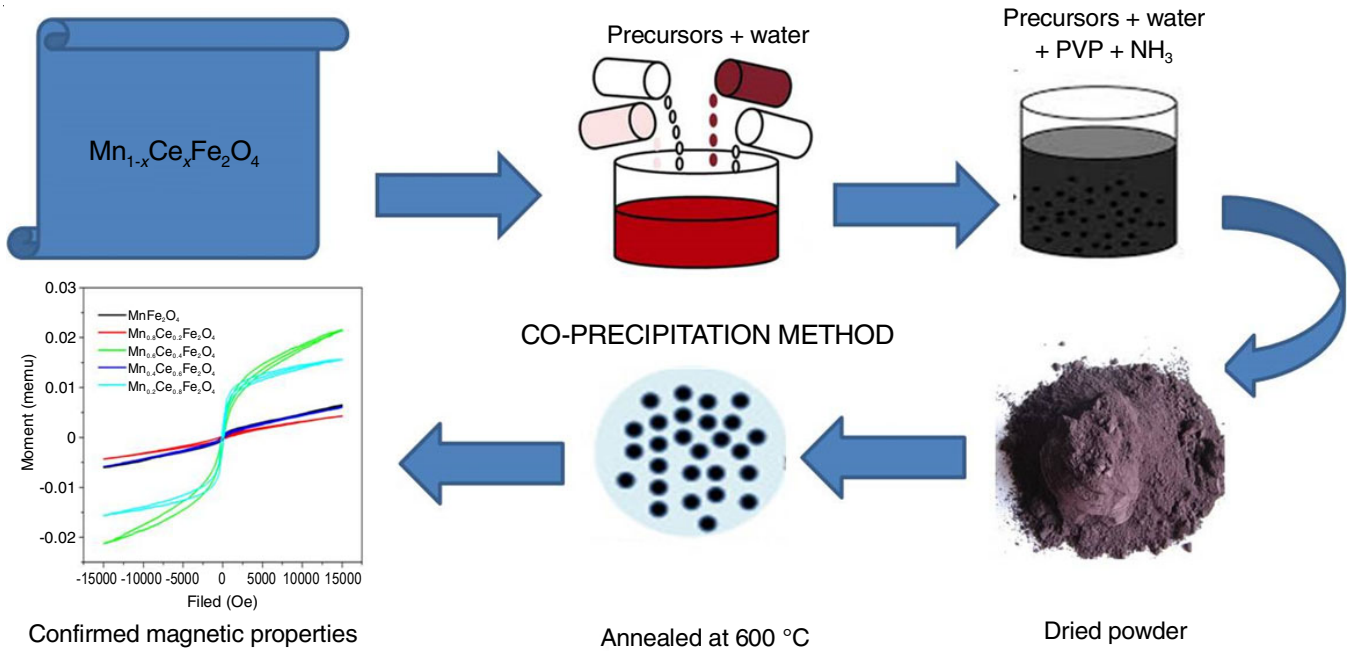

Fig. 1. Synthetic route of cerium doped manganese ferrites

RESULTS AND DISCUSSION

Structural analysis: Powder XRD patterns of cerium doped cubic phase ferrite system is shown in Fig. 2. The prominent diffraction peak observed at 2θ = 35.6º for the lattice plane (311) confirmed the formation of ferrite. XRD patterns of all samples showed well-defined peaks at 24.10º, 28.60º, 33.33º, 35.60º, 40.90º, 43.42º, 47.60º, 49.50º, 54.06º, 57.60º, 62.40º and 63.90º corresponding to the lattice plane of (210), (111), (222), (311), (411), (400) (220), (431), (430), (510), (511), (440) and (441), respectively. The reflection patterns are unique, definitely delineating the cubic phase of the spinels system [20]. Compare and observed pure diffraction peak with doped concentration such as $Mn_{0.8}Ce_{0.2}Fe_2O_4$, $Mn_{0.6}Ce_{0.4}Fe_2O_4$, $Mn_{0.4}Ce_{0.6}Fe_2O_4$ and $Mn_{0.2}Ce_{0.8}Fe_2O_4$ and their peak position shift to lower diffraction angles (2θ). The crystallite size of all the samples are ranged from 17 to 20 nm (Table-1). The ferrite materials are unaffected by these nanosized, as evidenced by the strain value (0.0069) of the first three samples. The ferrite system is highly influenced by Ce^{3+} integrated $MnFe_2O_4$ when cerium concentration is increased (x = 0.6). As a result, the crystallite size was increased to 20, when compared to pure crystallite size as shown in the Fig. 3. As Ce^{3+} is more increased in the pure like x = 0.0, ferrite materials decrease crystallite size (x = 0.8). For a bigger ionic radius of dopant ions (Mn^{2+} = 0.83 Å, Fe^{3+} = 0.65 Å, Ce^{3+} = 1.14 Å, Ce^{4+} = 0.97 Å) has stronger restraint effect than a smaller ionic radius [21]. With addition of Ce^{3+} ions in the pure materials, the lattice constant begins to decrease from 8.352 Å in the pure $MnFe_2O_4$ to 8.341 Å at Ce^{3+} loading. It denotes a drop in lattice constant when crystallite size decreases. First reason, a divalent ion (Mn^{2+}) was replaced by a trivalent ion (Ce^{3+}), which impeded crystal formation. Second, Ce^{3+}-O^{2-} has higher bond energy than Fe^{3+}-O^{2-}, since more energy is required to drive Ce^{3+} ions into the lattices to form the Ce^{3+}-O^{2-} bond. Although Ce^{3+} substituted ferrites

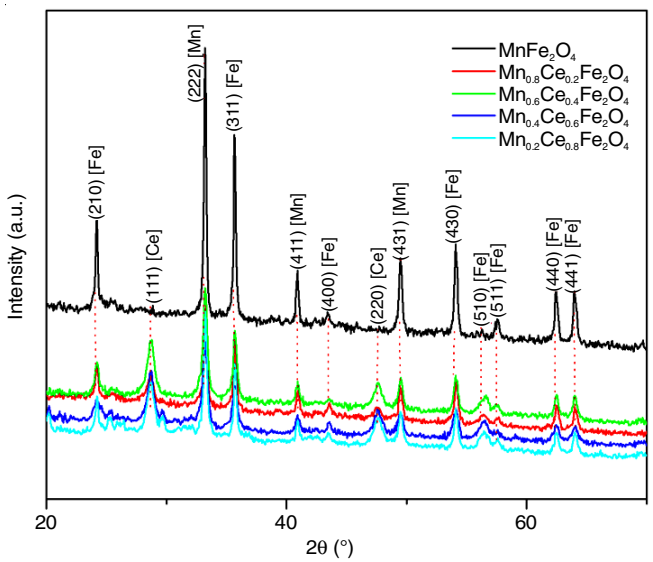

Fig. 2. XRD-powder pattern of cerium doped manganese ferrite $Mn_{1-x}Ce_xFe_2O_4$

TABLE-1
STRUCTURAL PROPERTIES OF
$Mn_{1-x}Ce_xFe_2O_4$ FERRITE NANOPARTICLES

Concentration (x)	2θ (°)	Crystallite size (D, nm)	Lattice constant (A, Å)	Strain (Δ)
0.0	35.65	17	8.352	0.0069
0.2	35.66	17	8.348	0.0069
0.4	35.68	17	8.345	0.0069
0.6	35.67	20	8.346	0.0057
0.8	35.69	17	8.341	0.0069

(x = 0.2, 0.4, 0.6, 0.8) have a greater thermal decomposition or thermal stability than pure ferrites (x = 0). For $Mn_{0.8}Ce_{0.2}Fe_2O_4$, $Mn_{0.6}Ce_{0.4}Fe_2O_4$, $Mn_{0.4}Ce_{0.6}Fe_2O_4$ and $Mn_{0.2}Ce_{0.8}Fe_2O_4$, more energy is required to complete grain crystallization and growth [22].

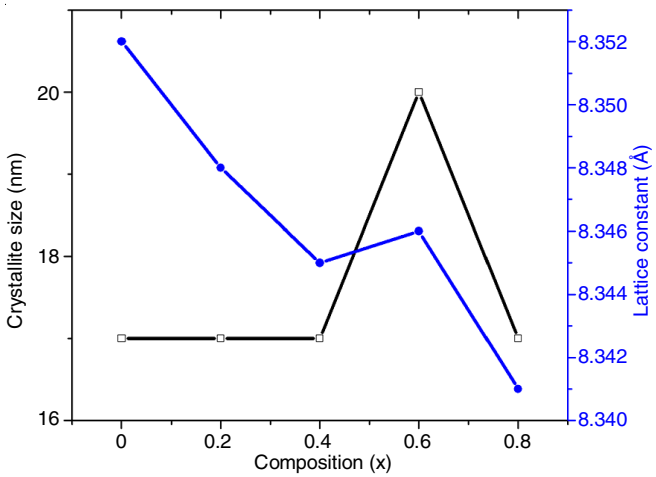

Fig. 3. Variation of the lattice constant of $Mn_{1-x}Ce_xFe_2O_4$ ferrites

Vibrational band analysis: Fig. 4 depicts the FTIR spectra of $Mn_{1-x}Ce_xFe_2O_4$ ferrite materials, which were used to analyze various vibrational bands. Here, there are two metal complexes vibrational band appeared at high wavenumbers in A-sites (ν_1: 585-554 cm^{-1}/Fe^{3+}-O^{2-}) and low wavenumber in the B-sites (ν_2: 477-460 cm^{-1}/M-O) [23,24]. This vibrational coordination was confirmed by spinel structure ferrite. In pure $MnFe_2O_4$, the functional groups incorporating Ce^{3+} is strongly affected by the band from 897 to 797 cm^{-1} [25]. Symmetric stretching vibration band from 1628 to 1529 cm^{-1} [26]. For antisymmetric stretching, the vibration band is attributed from 1140 to 1102 cm^{-1} [27]. Finally, the broad band appeared from 3438 cm^{-1} to 3213 cm^{-1} shows the presence of O-H stretching due to absorbed water and alcohol molecules [28].

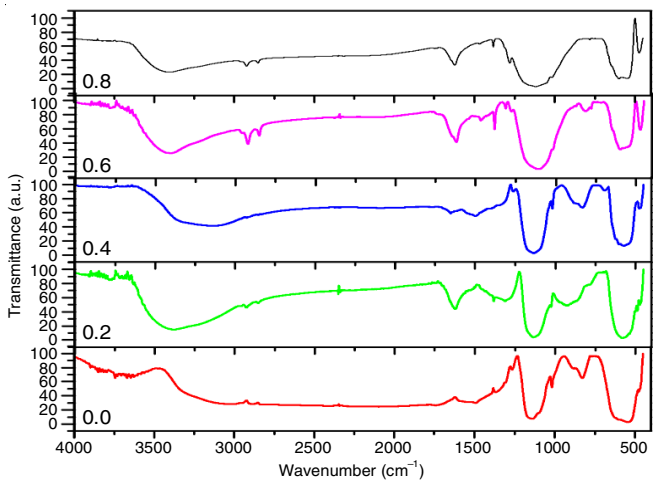

Fig. 4. FTIR spectra of cerium doped manganese ferrite $Mn_{1-x}Ce_xFe_2O_4$

Magnetic properties: Fig. 5 shows the plot of moment *versus* applied field of $Mn_{1-x}Ce_xFe_2O_4$ materials at room temperature. Hysteresis loops have well-defined S-shaped curves and a soft magnetic character that has been confirmed. Non-linear forms, reversible characterize, coercivity and mild retentivity were also seen in these curves. The magnetic characteristics of ferrites have been found to be influenced by interactions between A-B exchange, cation substitution and grain size. By

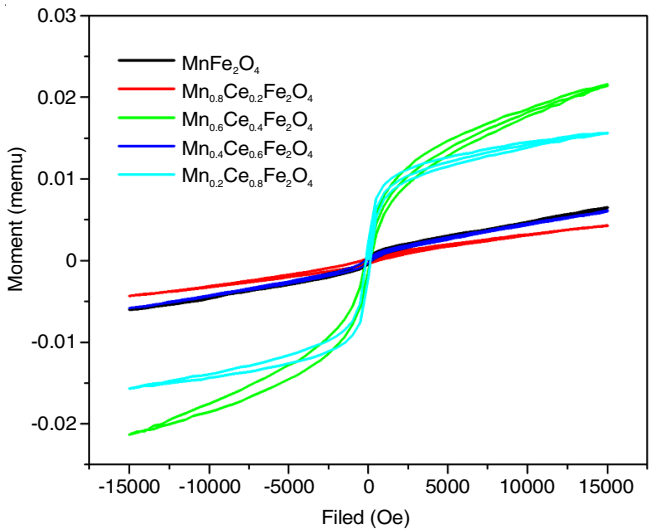

Fig. 5. VSM analysis at room temperature and hysteresis loops

increasing the amount of cerium and replacing Fe^{3+} ions with Ce^{3+} ions. Since, the interaction of the sub-lattice weakens with magnetic moments of the single domain diminish, lowering saturation magnetization (M_s) and coercivity (H_c) [24,25]. When the super exchange interaction (A-B) decreased, a spinning occurs on the nanosurface, magnetic characteristics to decrease all prepared samples [29,30]. So, a magnetic behaviour material depends not only on the changing particle size, but also on the doping concentration. The magnetic characteristics of all Ce^{3+} substituted ferrites were significantly impacted. Table-2 summarizes the magnetic properties that have been determined. Ferrites (x = 0.4 & 0.8) have higher saturation magnetization (M_s) than pure and x = 0.2 & 0.6 due to doping concentrations (Ce^{3+}) in the pure. Saturation magnetization decreases as cerium concentration increases for x = 0.0, 0.2 and 0.6 as shown in Fig. 6. This difference is caused by Ce^{3+} ions being replaced by Fe^{3+} ions in the B-sites [31,32], where x = 0.0, 0.2 & 0.4 have low magnetic moment 0.0743×10^{-3}, 0.0509×10^{-6}, 0.0556×10^{-3}, respectively. They are suggests the formation of hematite magnetic properties. The sample, x = 0.6 (0.0709×10^{-3}) and x = 0.8 (0.1896×10^{-3}) suggested the mixed hematite and ferrite magnetic signature. The magnetization and magnetic moment of x = 0.0, 0.2 and 0.6 samples decrease as the particle size and the surface ratio spins increases [7]. Cerium doped materials that have a soft nature have lower saturation magnetization, coercivity; remnant magnetization and remnant ratio [8].

TABLE-2
MAGNETIC PROPERTIES OF
$Mn_{1-x}Ce_xFe_2O_4$ FERRITE NANOPARTICLES

Conc. (x)	M_S $\times 10^{-3}$ (emu/g)	H_c (Oe)	M_r $\times 10^{-3}$ (emu/g)	μ_B $\times 10^{-3}$ Tesla	R
0.0	6.267	258.73	0.459	0.0743	0.07
0.2	4.291	511.92	0.316	0.0509	0.07
0.4	21.449	151.45	1.380	0.0556	0.06
0.6	5.977	222.77	0.303	0.0709	0.05
0.8	15.652	142.39	2.071	0.1896	0.13

Saturation magnetization (M_s), retentivity (M_r), coercivity (H_c), magnetic moment (μ_B) B = M × [MS/5585], remnant ratio (R = M_r/M_s), anisotropy constant (K) and energy product (E_p).

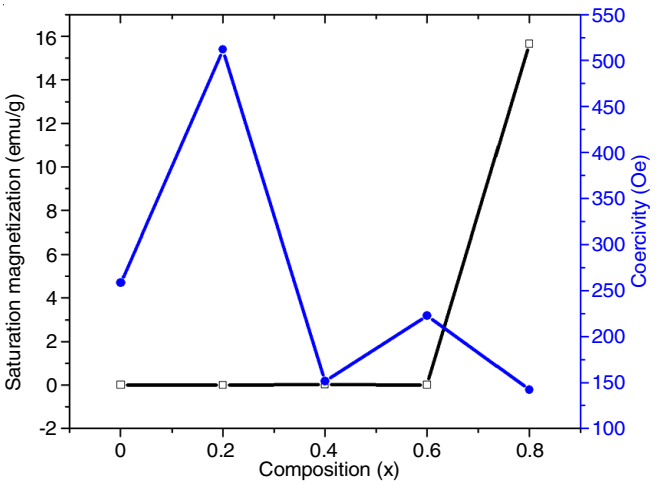

Fig. 6. Variation of saturation magnetization and coercivity values of $Mn_{1-x}Ce_xFe_2O_4$ ferrites

FE-SEM studies: Pure and doped samples investigate the surface morphology of $Mn_{1-x}Ce_xFe_2O_4$ nanoparticles by FE-SEM micrographs. It is confirmed that the chemical composition of synthesized sample using the EDX spectra got during the FE-SEM investigation. The FE-SEM micrograph of pure and other prepared samples (x = 0.0, 0.2, 0.4, 0.6 and 0.8) show ferrite samples with varying cerium concentrations (Fig. 7). All the prepared samples revealed the evenly distributed cerium spheres throughout the surface of MCF ferrite nanoparticles. The appearance of bright spots in the FE-SEM micrographs clarifies its welds together with two separate nanoparticles [20,33]. And also, the elements present in the pure and doped Ce^{3+} samples through the EDX spectra as shown in Fig. 8. As a result, the current work shows the purity of nanoparticles generated using the co-precipitation approach.

X-ray photoelectron spectroscopic studies: Fig. 9 shows the XPS wide-scan spectra of $Mn_{1-x}Ce_xFe_2O_4$ (MCF) ferrite nanoparticles. Since, the binding energy of distinct elements varies, the binding energy measurements are used to determine which elements are present in the samples. A survey scan of the samples shows elements such as oxygen, iron, manganese and cerium.

Mn 2p peak: They exhibited Mn 2*p* spectra of $Mn_{1-x}Ce_xFe_2O_4$ (MCF) ferrite nanoparticles with excellent resolution in Fig. 10. $MnFe_2O_4$ has two prominent peaks around 642.14 eV (Mn $2p^{3/2}$) and 653.89 eV (Mn $2p^{1/2}$) in the XPS spectra that correspond to Mn 2p. Using the Lorentzian-Gaussian model [22], the peak position of Mn 2p spectra was calculated. Between Mn $2p_{3/2}$ and Mn $2p_{1/2}$, no satellite peak is visible. This demonstrates the absence of manganese in Mn^{2+} state at the surface [34]. No new peaks have appeared as a result of Ce substitution, indicating that Ce has been incorporated into the $Mn_{1-x}Ce_xFe_2O_4$.

Ce $3d_5$ peak: The Ce 3d spectra of $Mn_{1-x}Ce_xFe_2O_4$ (MCF) ferrite nanoparticles at high resolution are shown in Fig. 11. The Lorentzian-Gaussian model was used to match the peak

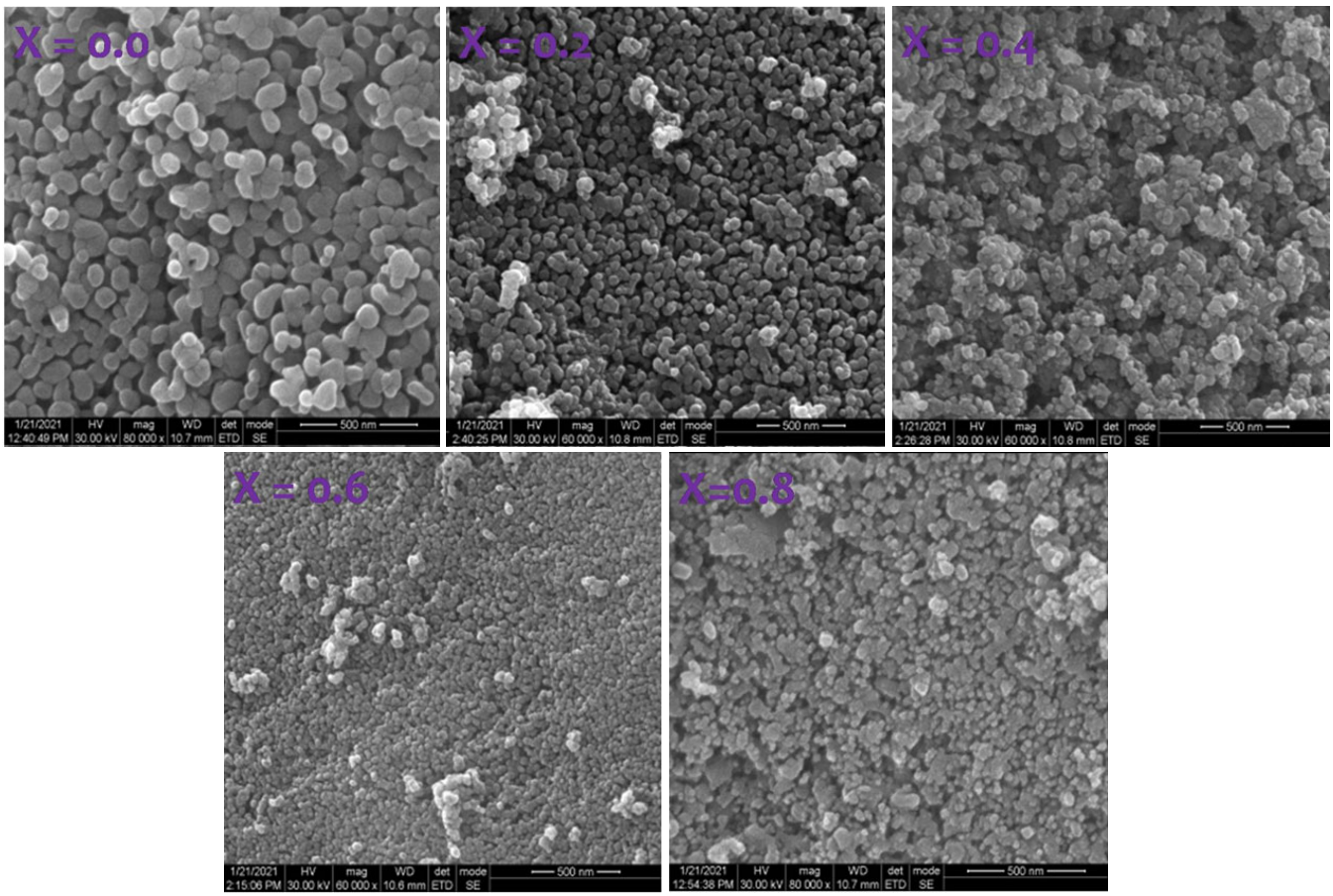

Fig. 7. FE-SEM morphology analysis of cerium doped manganese ferrite $Mn_{1-x}Ce_xFe_2O_4$

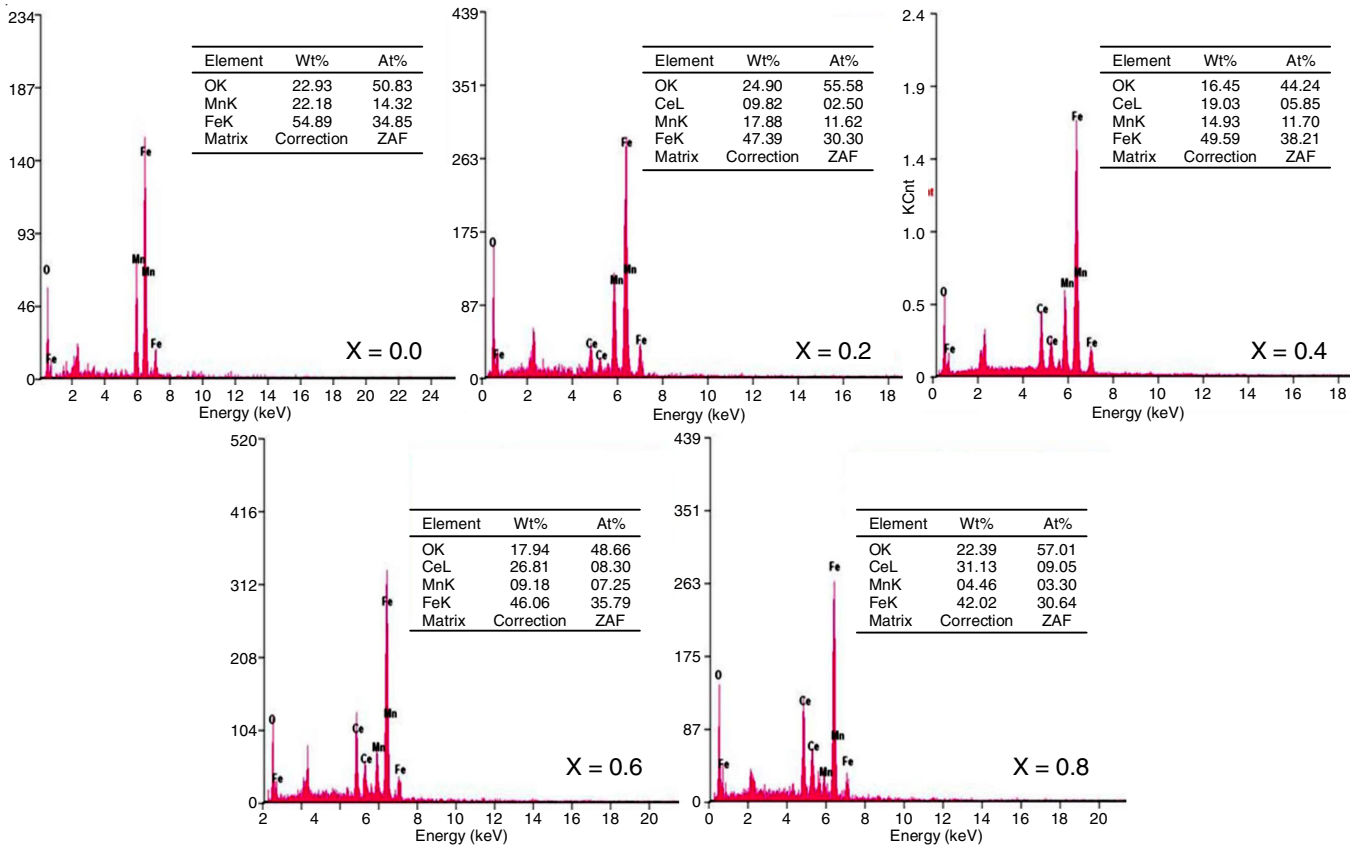

Fig. 8. FE-SEM morphology analysis of cerium doped maganize ferrite $Mn_{1-x}Ce_xFe_2O_4$

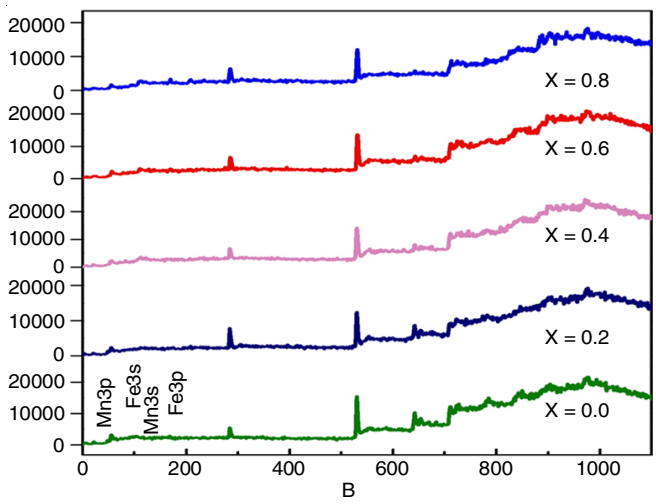

Fig. 9. XPS spectra of $Mn_{1-x}Ce_xFe_2O_4$ mixed ferrite nanoparticles

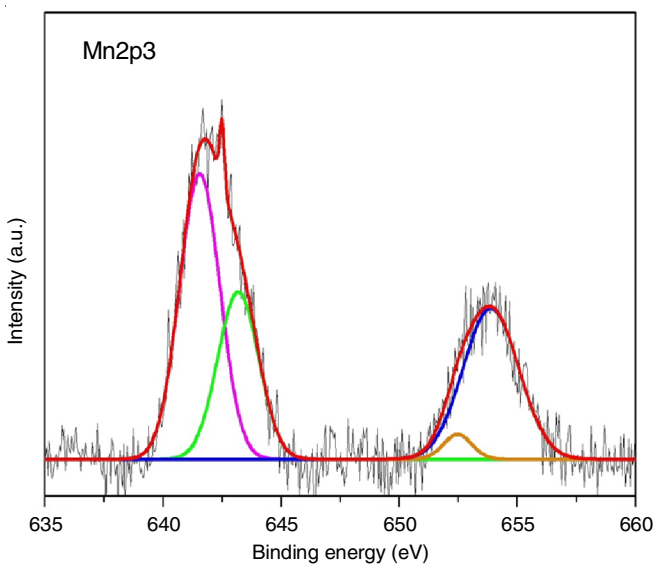

Fig. 10. Mn 2p XPS spectra of nanocrystalline $Mn_{1-x}Ce_xFe_2O_4$ mixed ferrites

positions of the Ce ions in Ce 3d spectra. Peak positions of the Ce 3d with binding energy values of 284.76 eV were detected, demonstrating the presence of Ce^{2+} ion [35]. These spectra show that it completely dissolved the Ce atom in $Mn_{1-x}Ce_xFe_2O_4$ with a spinel structure.

Fe 2p peak: Fig. 12 shows the high-resolution Fe 2p spectra of MCF ferrite nanoparticles. The binding energies of Fe $2p_{3/2}$ and Fe $2p_{1/2}$ were 711.31 eV and 724.90 eV, respectively, in the XPS spectra. Furthermore, the satellite peaks arise around 734.30 eV binding energies, indicating the existence of Fe^{3+} cations [34]. The presence of Ce in nanocrystalline ferrite does not result in the formation of new peaks, showing that Ce has no effect on the ionic state of Fe.

O 1s peak: The Lorentzian-Gaussian model was used to fit the O 1s high-resolution spectra of $Mn_{1-x}Ce_xFe_2O_4$ ferrite nanoparticles. The major peaks (Fig. 13) for O 1s with binding energies of 284.05 eV, 528.34 eV, 637.49 eV, 728.74 eV, 783.31 eV, 848.86 eV and 907.19 eV were detected. The metal cations doubly bound with metal-oxygen atoms have a peak at 529.54 eV. The cation covalently attributed to two atoms [36] has a

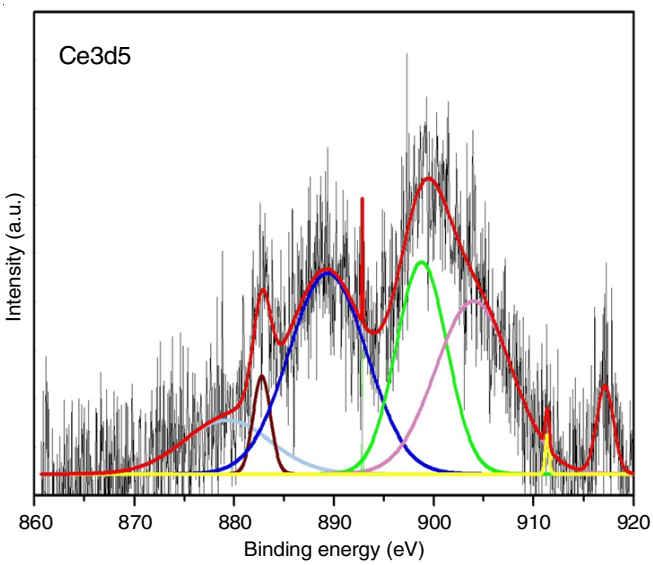

Fig. 11. Ce 3d5 XPS spectra of nanocrystalline $Mn_{1-x}Ce_xFe_2O_4$ mixed ferrite

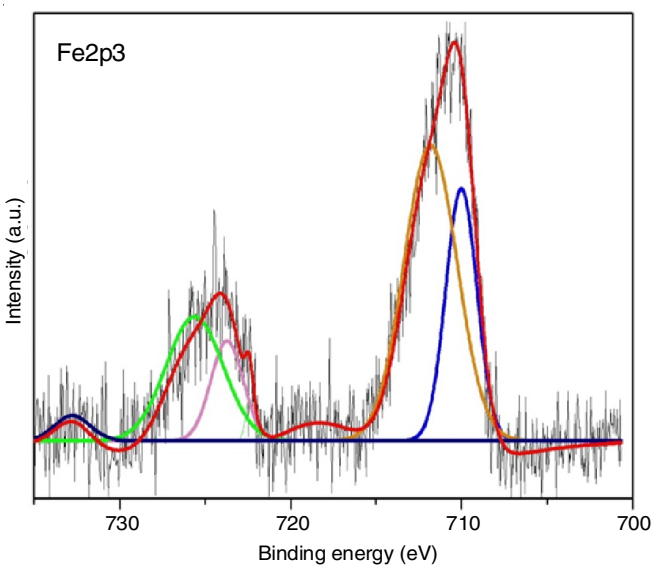

Fig. 12. Fe2p XPS spectra of nanocrystalline $Mn_{1-x}Ce_xFe_2O_4$ mixed ferrites

peak at 530.78 eV. The binding energy of nanocrystalline $Mn_{1-x}Ce_xFe_2O_4$ ferrites was increased by the addition of Ce.

Antibacterial activity: The antibacterial activity of the synthesized $Mn_{1-x}Ce_xFe_2O_4$/PVP (MCF) samples were evaluated against both Gram-negative and Gram-positive microorganisms. The nanoparticles have the ability to reach the microbial nucleus intracellular due to electrostatic force [12]. The Gram-

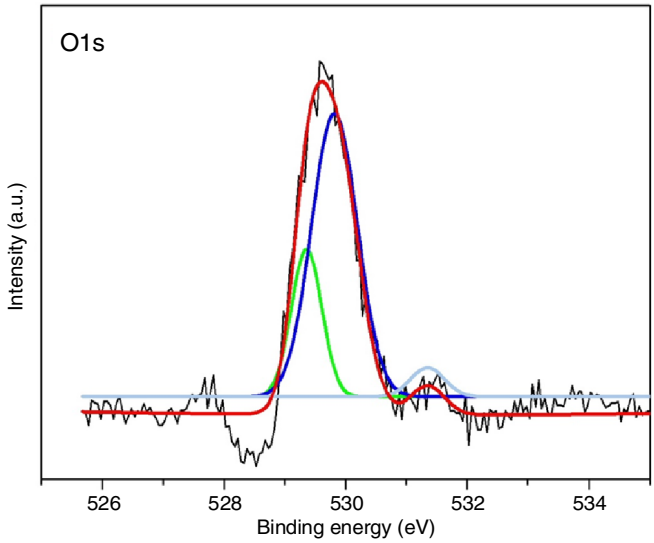

Fig. 13. O 1s XPS spectra of nanocrystalline $Mn_{1-x}Ce_xFe_2O_4$ mixed ferrites

positive bacteria has a cell wall of *Bacillus cereus* (55.4 nm) [2], *Bacillus subtilis* (20-40 nm) [37], *Staphylococcus petrasii subs. pragensis* (0.5-1.8 nm) [38], while the Gram-negative bacteria has a cell wall *Enterobacter cloacae* (~3.5 cm) [39], *Escheichia coli* (0.25-1.0 µm) [40], *Staphylococus haemolytics* (0.8-1.3 µm) [41]. The test bacteria such as Gram-negative bacteria and Gram-positive bacteria are used in antibacterial study. Initially, the petriplates were marked as bacteria loading from 12.5 µg/mL, 25 µg/mL, 50 µg/mL, 75 µg/mL and 100 µg/mL for five different petri-plates. Microbial colonies (zone of inhibition) were observed for different bacteria and are shown in Table-3. Microbial colonies were well indicated that the material effectively worked as antibacterial agent for tested microorganisms. As cerium concentration rises, the zone of inhibitory colonies increases. For higher concentrations have higher antibacterial activity than lower Ce doped concentrations. The nanocrystallites (17-20 nm) have superparamagnetism phase which is thermally active in the vicinity of membranes [12,18]. For all bacteria, the zone of inhibition is severely influenced, ranging from 11 mm to 14 mm for higher loading of 100 µg/mL and 75 µg/mL, respectively. As compared to other bacteria, *Staphylococcus haemolyticus* and *Bacillus subtilis* have all concentrations suppressed. These observations demonstrate that cell death has an anti-concentration effect. Hence, antibacterial activity of the synthesized $Mn_{1-x}Ce_xFe_2O_4$ ferrite nanoparticles was observed to be increased at a greater rate and can be used for the biomedical applications.

TABLE-3
TEST ORGANISMS OF GRAM-NEGATIVE AND GRAM-POSITIVE BACTERIA

Test organism	Zone of inhibition (mm)					
	100 µg/mL (x = 0.8)	75 µg/mL (x = 0.6)	50 µg/mL (x = 0.4)	25 µg/mL (x = 0.2)	12.5 µg/mL (x = 0.0)	Control
Enterobacter cloacae	13	12	10	–	–	20
Escheichia coli	13	11	–	–	–	21
Staphylococus haemolytics	14	13	12	8	7	20
Bacillus cereus	13	12	11	–	–	21
Bacillus subtilis	14	13	12	9	7	20
Staphylococcus petrasii sub s.pragensis	13	12	9	–	–	22

Conclusion

This work discussed the influence of cerium ions (Ce^{3+}) substitution on the structural, morphological, magnetic properties and antibacterial activity of the prepared $Mn_{1-x}Ce_xFe_2O_4$ ferrite samples. The XRD data revealed the cubic structure and crystallite size range from 17 to 20 nm. FTIR studies also confirmed the ferrite formation due to the tetrahedral (477-460 cm^{-1}) and octahedral (585-554 cm^{-1}) vibrational modes. The FE-SEM micrographs reflect the bright spots and spherical morphology. The EDAX spectra also confirmed purity of the materials, weight percentage and atomic percentage. The VSM clearly showed that all samples exhibit soft magnetic nature since $MnFe_2O_4$ has quite low magnetic moment and therefore resulted in the formation of hematite. Moreover, the higher Ce^{3+} doped concentrations (x = 0.8), ferrite material exhibited higher antibacterial inhibition zone (13-14 mm) as compared to the lower Ce^{3+} doped concentrations (x = 0.2).

ACKNOWLEDGEMENTS

The authors are grateful to the Nanotechnology and Crystal Growth Lab, Department of Physics, St. Joseph's College of Arts and Science (Autonomous), Cuddalore, India for providing the research lab facilities.

CONFLICT OF INTEREST

The authors declare that there is no conflict of interests regarding the publication of this article.

REFERENCES

1. O.L. Pop, A. Mesaros, D.C. Vodnar, R. Suharoschi, L. Magerusan, I.S. Tódor, F. Tăbăran, Z. Diaconeasa, A. Balint, L. Ciontea and C. Socaciu, *Nanomaterials*, **10**, 1614 (2020); https://doi.org/10.3390/nano10081614
2. M. Zhang, C. Zhang, X. Zhai, F. Luo, Y. Du and C. Yan, *Sci. China Mater.*, **62**, 1727 (2019); https://doi.org/10.1007/s40843-019-9471-7
3. S.K. Kannan and M. Sundrarajan, *Int. J. Nanosci.*, **13**, 1450018 (2014); https://doi.org/10.1142/S0219581X14500185
4. K.R. Singh, V. Nayak, T. Sarkar and R.P. Singh, *RSC Adv.*, **10**, 27194 (2020); https://doi.org/10.1039/D0RA04736H
5. N. Thakur, P. Manna and J. Das, *J. Nanobiotechnology*, **17**, 84 (2019); https://doi.org/10.1186/s12951-019-0516-9
6. E. Alpaslan, B.M. Geilich, H. Yazici and T.J. Webster, *Sci. Rep.*, **7**, 45859 (2017); https://doi.org/10.1038/srep45859
7. H. Yamamura, H. Haneda, S.I. Shirasaki and K. Takada, *J. Solid State Chem.*, **36**, 1 (1981); https://doi.org/10.1016/0022-4596(81)90185-7
8. A. Hashhash, I. Bobrikov, M. Yehia, M. Kaiser and E. Uyanga, *J. Magn. Magn. Mater.*, **503**, 166624 (2020); https://doi.org/10.1016/j.jmmm.2020.166624
9. S.I. Ahmad, D.R. Kumar, I.A. Syed, R. Satar and S.A. Ansari, *J. Appl. Sci. Eng.*, **42**, 389 (2017); https://doi.org/10.1007/s13369-016-2297-x
10. M. Kurian and C. Kunjachan, *Int. Nano Lett.*, **4**, 73 (2014); https://doi.org/10.1007/s40089-014-0122-7
11. R. Sagayaraj, S. Aravazhi, C. Selva kumar, S. Senthil kumar and G. Chandrasekaran, *SN Appl. Sci.*, **1**, 271 (2019); https://doi.org/10.1007/s42452-019-0244-7
12. R. Sagayaraj, T. Dhineshkumar, A. Prakash, G. Chandrasekaran, S. Aravazhi, D. Jayarajan and S. Sebastian, *Chem. Phys. Lett.*, **759**, 137944 (2020); https://doi.org/10.1016/j.cplett.2020.137944
13. T. Shalaby, H. Hamad, E. Ibrahim, O. Mahmoud and A. Al-Oufy, *Ecotoxicol. Environ. Saf.*, **162**, 354 (2018); https://doi.org/10.1016/j.ecoenv.2018.07.016
14. S. Rajeshkumar and P. Naik, *Biotechnol. Rep.*, **17**, 1 (2018); https://doi.org/10.1016/j.btre.2017.11.008
15. R. Zalneravicius, A. Paskevicius, M. Kurtinaitiene and A. Jagminas, *J. Nanopart. Res.*, **18**, 300 (2016); https://doi.org/10.1007/s11051-016-3612-x
16. A. Santhoshkumar, H.P. Kavitha and R. Suresh, *Karbala Int. J. Mod. Sci.*, **2**, 196 (2016); https://doi.org/10.1016/j.kijoms.2016.06.001
17. K. Gopinath, V. Karthika, C. Sundaravadivelan, A. Arumugam and S. Gowri, *J. Nanostruct. Chem.*, **5**, 295 (2015); https://doi.org/10.1007/s40097-015-0161-2
18. E.O. Gubernatorova, X. Liu, A. Othman, W.T. Muraoka, E.P. Koroleva, S. Andreescu and A.V. Tumanov, *Adv. Healthcare Mater.*, **6**, 1700176 (2017); https://doi.org/10.1002/adhm.201700176
19. N. Yasmin, S. Abdulsatar, M. Hashim, M. Zahid, S. Fatima Gillani, A. Kalsoom, M. Naeem Ashiq, I. Inam, M. Safdar and M. Mirza, *J. Magn. Magn. Mater.*, **473**, 464 (2019); https://doi.org/10.1016/j.jmmm.2018.10.076
20. T. Pandiarajan, S. Ravichandran and L.J. Berchmans, *RSC Adv.*, **4**, 64364 (2014); https://doi.org/10.1039/C4RA09806D
21. S. Yang, D. Han, Z. Wang, Y. Liu, G. Chen, H. Luan, L. Bayanheshig and L. Yang, *Mater. Sci. Semicond. Process.*, **27**, 854 (2014); https://doi.org/10.1016/j.mssp.2014.08.032
22. B. Yan, P. Gao, Z. Lu, R. Ma, E.V. Rebrov, H. Zheng and Y. Gao, *J. Alloys Compd.*, **639**, 626 (2015); https://doi.org/10.1016/j.jallcom.2015.03.211
23. A. Anantharaman, T.L. Ajeesha, J.N. Baby and M. George, *Solid State Sci.*, **99**, 105846 (2020); https://doi.org/10.1016/j.solidstatesciences.2019.02.007
24. S. Ikram, J. Jacob, K. Mahmood, A. Ali, N. Amin, U. Rehman, M.I. Arshad, M. Ajaz un Nabi, K. Javid, A. Ashfaq, M. Sharif and S. Hussain, *Physica B*, **41**, 1764 (2019); https://doi.org/10.1016/j.physb.2019.411764
25. M.A. Rehman, I. Yusoff and Y. Alias, *Ceram. Int.*, **42**, 1399 (2016); https://doi.org/10.1016/j.ceramint.2015.09.083
26. T. Roman, A. Pui, A.V. Lukacs, N. Cimpoesu, S. Lupescu, A.I. Borhan, K. Kordatos, A. Ntziouni, P. Postolache, M. Zaharia, S. Stanciu and L. Mitoseriu, *Ceram. Int.*, **45**, 17243 (2019); https://doi.org/10.1016/j.ceramint.2019.05.280
27. W. Gu, Q. Xie, M. Xing and D. Wu, *Chem. Eng. Res. Des.*, **117**, 706 (2017); https://doi.org/10.1016/j.cherd.2016.11.026
28. R. Álvarez-Asencio, R.W. Corkery and A. Ahniyaz, *RSC Adv.*, **10**, 14818 (2020); https://doi.org/10.1039/D0RA01710H
29. R. Sagayaraj, S. Aravazhi and G. Chandrasekaran, *Int. Nano Lett.*, **11**, 307 (2021); https://doi.org/10.1007/s40089-021-00343-z
30. J. Peng, M. Hojamberdiev, Y. Xu, B. Cao, J. Wang and H. Wu, *J. Magn. Magn. Mater.*, **323**, 133 (2011); https://doi.org/10.1016/j.jmmm.2010.08.048
31. R. Sagayaraj, S. Aravazhi and G. Chandrasekaran, *J. Inorg. Organomet. Polym. Mater.*, **29**, 2252 (2019); https://doi.org/10.1007/s10904-019-01183-3
32. R. Sagayaraj, S. Aravazhi and G. Chandrasekaran, *Appl. Phys., A Mater. Sci. Process.*, **127**, 502 (2021); https://doi.org/10.1007/s00339-021-04653-z
33. M.A. Almessiere, Y. Slimani and A. Baykal, *J. Rare Earths*, **38**, 188 (2020); https://doi.org/10.1016/j.jre.2019.07.005
34. Y. Fu, P. Xiong, H. Chen, X. Sun and X. Wang, *Ind. Eng. Chem. Res.*, **51**, 725 (2012); https://doi.org/10.1021/ie2026212

35. S. Al Khabouri, S. Al Harthi, T. Maekawa, Y. Nagaoka, M.E. Elzain, A. Al Hinai, A.D. Al-Rawas, A.M. Gismelseed and A.A. Yousif, *Nanoscale Res. Lett.*, **10**, 262 (2015); https://doi.org/10.1186/s11671-015-0971-7
36. J. Bennet, R. Tholkappiyan, K. Vishista, N.V. Jaya and F. Hamed, *Appl. Surf. Sci.*, **383**, 113 (2016); https://doi.org/10.1016/j.apsusc.2016.04.177
37. A.M. Glauert, E.M. Brieger and J.M. Allen, *Exp. Cell Res.*, **22**, 73 (1961); https://doi.org/10.1016/0014-4827(61)90087-8
38. R. Pantucek, P. Svec, J.J. Dajcs, I. Machová, J. Cernohlávková, O. Sedo, T. Gelbícová, I. Maslacová, J. Doskar, Z. Zdráhal, V. Ruzicková and I. Sedlácek, *Syst. Appl. Microbiol.*, **36**, 90 (2013); https://doi.org/10.1016/j.syapm.2012.11.004
39. H. Hoffmann, E. Stürenburg, J. Heesemann and A. Roggenkamp, *Clin. Microbiol. Infect.*, **12**, 322 (2006); https://doi.org/10.1111/j.1469-0691.2006.01360.x
40. N. Ouzounov, J.P. Nguyen, B.P. Bratton, D. Jacobowitz, Z. Gitai, J.W. Shaevitz and B. Mre, *Biophys. J.*, **111**, 1035 (2016); https://doi.org/10.1016/j.bpj.2016.07.017
41. A. Nunes, L. Teixeira, N. Iorio, C. Bastos, L. Fonseca, T. Soutopadron and K. Dossantos, *Int. J. Antimicrob. Agents*, **27**, 307 (2006); https://doi.org/10.1016/j.ijantimicag.2005.11.013